Potential Vorticity and Layer Thickness Variations in the Flow around Jupiter's Great Red Spot and White Oval BC*

TIMOTHY E. DOWLING AND ANDREW P. INGERSOLL

Division of Geological and Planetary Sciences, California Institute of Technology, Pasadena, California

(Manuscript received 10 April 1987, in final form 2 December 1987)

ABSTRACT

Layer thickness variations in Jupiter's atmosphere are investigated by treating potential vorticity as a conserved tracer. Starting with the horizontal velocity field measured from *Voyager* images, fluid trajectories around the Great Red Spot (GRS) and White Oval BC are calculated. The flow is assumed to be frictionless, adiabatic, hydrostatic, and steady in the reference frame of the vortex. Absolute vorticity is followed along each trajectory; its magnitude is assumed to vary directly as the thickness, which is defined as the mass per unit area between potential temperature surfaces. To the accuracy of the observations, the inferred thickness is a separable function of trajectory and latitude. The latitude dependence has positive curvature near the GRS and BC. The relative variations of thickness with respect to latitude are generally larger than the relative variations of Coriolis parameter with respect to latitude—the beta effect. The data are a useful diagnostic which will help differentiate between models of Jovian vortices. The present analysis employs a quasi-geostrophic model in which a thin upper weather layer, which contains the vortex, is supported hydrostatically by a much deeper lower layer. In this model, the upper free surface does not contribute to the observed variation of thickness along trajectories. Such variations are due exclusively to bottom topography—flow of the deep lower layer relative to the vortex. The observations are used to infer the form of the deep zonal velocity profile vs. latitude. The magnitude of the profile depends on the unknown static stability. The principal result is the existence of horizontal shear in the deep layer zonal velocity profile, i.e., the lower layer is not in solid body rotation and does not act like a flat solid surface. In this respect the data support the hypothesis of Ingersoll and Cuong concerning motions in the deep layer. However at some latitudes the data violate Ingersoll and Cuong's criterion governing the compactness of the vortices. At these latitudes the topography allows standing Rossby waves (wakes) extending far downstream to the west. Observed wavelike features, the filamentary regions, are possibly formed by this mechanism.

1. Introduction

The effect of vertical structure on large-scale atmospheric flows is summarized by the principle of conservation of potential vorticity. For adiabatic, hydrostatic, frictionless flow in a stably stratified fluid, the important vertical variable is the thickness (actually the mass per unit area) of a layer bounded above and below by surfaces of constant potential temperature. The principle states that as a fluid parcel moves within such a layer, the ratio between the parcel's absolute vorticity and its thickness remains constant. On Jupiter absolute vorticity is calculated directly from the horizontal wind field, which is measured by tracking clouds in *Voyager* images. The trajectories of fluid parcels are also calculated from the wind field. Therefore, by following the changes of absolute vorticity along the fluid trajectories, one can measure the shape of potential temperature surfaces in Jupiter's atmosphere.

We define potential vorticity as $(\zeta + f)/H$. Here ζ is $\mathbf{k} \cdot \nabla \times v$, the vertical component of relative vorticity; f is planetary vorticity $2\Omega \sin\lambda$, where Ω is the planet's angular speed of rotation ($2\pi/\Omega = 9^h55^m29.7^s$) and λ is planetographic latitude; H is $-\partial P/\partial\theta$, the pressure thickness ΔP per unit change in potential temperature $\Delta\theta$. This is a special form of Ertel's (1942) potential vorticity. For large scale (hydrostatic), adiabatic, frictionless flow, it is a constant following the fluid motion (e.g., Holton 1979; Pedlosky 1987; Haltiner and Williams 1980). By plotting the absolute vorticity $(\zeta + f)$ as it changes along a trajectory, one can observe the relative changes of H. By observing such profiles we gain a detailed diagnostic which will help to differentiate between current models of Jovian vortices.

Absolute values of H cannot be determined without additional information, e.g., a measurement of temperature vs. pressure at some point along the trajectory. For Jupiter a direct measurement of $-\partial P/\partial\theta$ is difficult. The relevant levels are hidden in the clouds, whose tops are at 0.5 to 1.0 bars, and whose bottoms are perhaps at 3 to 5 bars (e.g., Ingersoll et al. 1984). Moreover, the departures of the profiles from an adiabat ($-\partial\theta/\partial P$

* Contribution number 4460 from the Division of Geological and Planetary Sciences, California Institute of Technology, Pasadena, California 91125.

Corresponding author address: Dr. Timothy E. Dowling, Division of Geological and Planetary Sciences, California Institute of Technology, Pasadena, CA 91125.

$= 0$) are likely to be small. Direct estimates of $-\partial P/\partial\theta$ are sensitive to the assumed composition, rates of conversion between ortho and para hydrogen, and to errors of observation. With data now in hand, potential vorticity provides perhaps the best method of gathering information about $-\partial P/\partial\theta$ at altitudes within the clouds.

The most interesting regions are those where meridional motion is occurring, since f will then vary along the trajectories. Examples include the flow around the Great Red Spot (GRS) and the three white ovals. Both the GRS and the white oval BC were studied during the Voyager encounters by Mitchell et al. (1981). They determined radial profiles of wind speed and vorticity on a set of concentric ellipses. Winds of order 110 to 120 m s^{-1} were found at the outer edges of both the GRS and BC. However, Mitchell et al. did not determine fluid trajectories, and did not discuss the variations of tangential velocity and vorticity around the circumferences.

We have expanded on the analysis of Mitchell et al. in several ways. First, we infer fluid trajectories directly from the data, without assuming that the trajectories are elliptical or closed. Second, we have combined *Voyager 1* and *Voyager 2* data, and included data taken when the spacecraft was farther from Jupiter in order to study a larger region around the GRS. Third, we have organized our data so as to bring out the variations of $(\zeta + f)$ along each trajectory.

There have been other quantitative studies of meridional motion on Jupiter. Hatzes et al. (1981) studied the divergence, vorticity, and oscillatory behavior of brown barges. The barges are cyclonic and exceptions to the rule that all long-lived, compact oval spots like the GRS and BC are anticyclonic (high pressure) regions. Mac Low and Ingersoll (1986) studied over 100 spots involved in mergings and other interactions, for spot sizes (major diameters) ranging from 500 to 7000 km. Several groups (Beebe et al. 1980; Ingersoll et al. 1981; Limaye et al. 1982; Sromovsky et al. 1982) have measured the eddy stress term $\overline{u'v'}$ and its relation to the ambient shear $d\bar{u}/dy$. These papers are discussed by Ingersoll et al. (1984) in their review of the dynamics of the atmospheres of Jupiter and Saturn.

The present paper is organized as follows: Section 2 describes the dataset. Section 3 gives the method of data analysis—how to extract information from a set of over 2000 velocity vectors measured at irregular locations with respect to latitude and longitude. Section 4 describes tests that were made to evaluate the uncertainty of our results. Section 5 presents a test of the physical model, based on the fact that the trajectories are closed to a good approximation. Section 6 gives the results of the data analysis. Finally, sections 7 and 8 discuss implications in the context of a quasi-geostrophic model similar to that of Ingersoll and Cuong (1981), in which variations of thickness along the trajectories arise from a deep zonal flow in the adiabatic layer beneath the clouds.

2. Dataset

The dataset for the GRS consists of over 2000 velocity vectors from the *Voyager 1* and *Voyager 2* encounters. The dataset for BC is just over 400 vectors from the *Voyager 1* encounter. Each vector is computed from the displacement of a feature that is visible in a pair of images separated in time. A human operator locates the feature; the program AMOS then computes the zonal and meridional velocities taking into account the oblate spheroidal shape of the planet and the spacecraft viewing geometry (Yagi et al. 1978). The error due to feature location is scene-dependent. In the best cases when the features are sharp and well-defined the error is about 2 pixels. The error due to viewing geometry (camera pointing uncertainty) is about 2 pixels in all cases, and is the same for all points in an image (Ingersoll et al. 1981).

The GRS data were derived from 10 image pairs separated in time by 10 hours and one image pair separated by 20 hours. The resolution ranged from 20 to 40 km/pixel. Most of the BC data (330 out of 429 vectors) come from a single pair separated by 1.4 hours at a resolution of 10 km/pixel. The other BC data come from pairs separated by 10 hours. In the best cases, the measurement error for velocity (four pixels divided by the time interval) is 2 to 4 m s^{-1} for the GRS and 8 m s^{-1} for BC. We excluded several *Voyager 1* pairs of the GRS taken 0.5 hours apart, since these have best-case errors of order 25 m s^{-1}. For comparison, peak velocities around the GRS and BC are over 100 m s^{-1}.

Each velocity vector is assigned a latitude and longitude from the averages of the latitudes and longitudes in the two images. We define planetographic latitude λ as the angle between the local vertical and its projection onto the equatorial plane, with equatorial and polar radii R_e and R_p of 71 400 and 66 773 km, respectively. Planetocentric latitude λ_c is related to λ by the equation $\tan\lambda = \epsilon^2 \tan\lambda_c$, where $\epsilon = R_e/R_p$. We use longitude ϕ, defined relative to the System III coordinate system rotating with the magnetic field of Jupiter.

Figure 1 is a *Voyager 2* image of the GRS (FDS 20517.32). The image is labeled with planetographic latitude and System III longitude (the actual projection is a Cartesian coordinate system with planetocentric latitude and longitude in equal increments along the two axes). *Voyager 1* images of the GRS and BC are shown in Mitchell et al. (1981). Figure 2 shows the measured velocities from *Voyager 1* and *Voyager 2* presented in the reference frame of the GRS. Figure 3 shows sample trajectories computed from Fig. 2, with small dots indicating intervals of 10 hours. Figures 4 and 5 show the measured velocities and corresponding trajectories for BC.

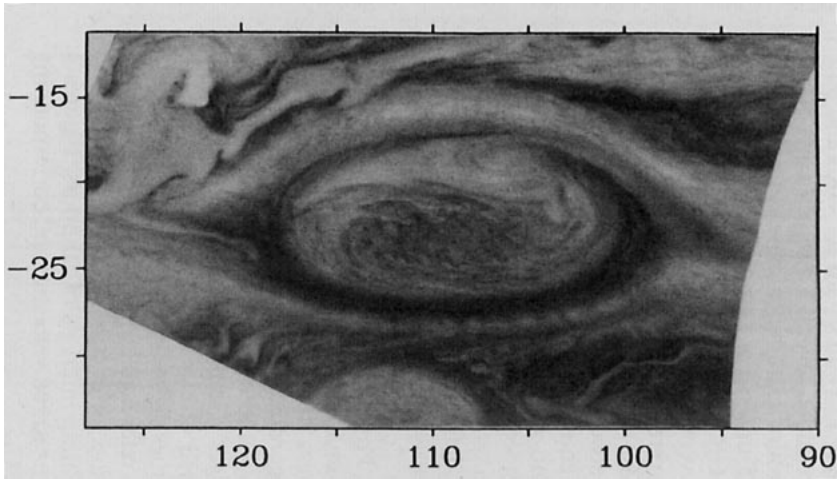

FIG. 1. *Voyager 2* image of the Great Red Spot (GRS) taken on 5 July 1979 (FDS 20517.32). All maps in this paper are labeled in degrees with planetographic latitude along the ordinate and System III longitude increasing westward along the abscissa. (In this image the actual projection is a Cartesian coordinate system with planetocentric latitude and longitude in equal increments along the two axes.)

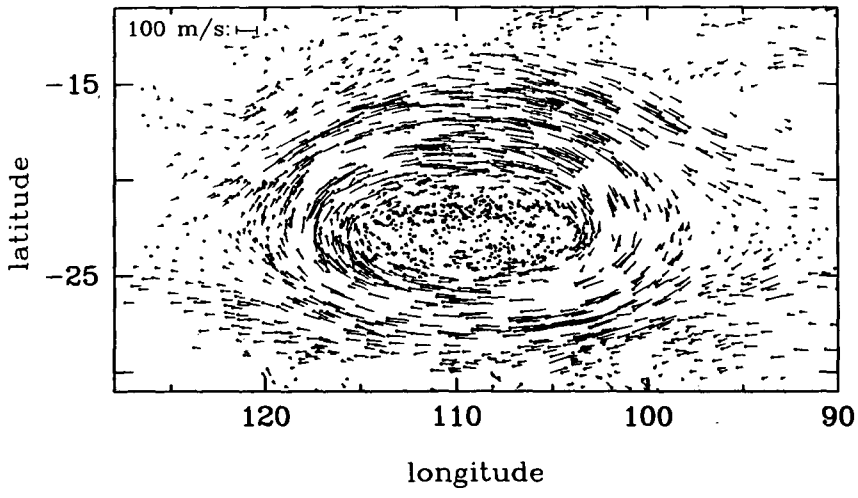

FIG. 2. Velocity data for the GRS. The location of each vector is marked with a dot, and the lines point downwind. The northward and eastward components of velocity are scaled equally in m s^{-1}, with 100 m s^{-1} indicated at the top left of the figure. Longitude and planetographic latitude are labeled in degrees and scaled equally, with the zero of longitude corresponding to System III on 5 July 1979.

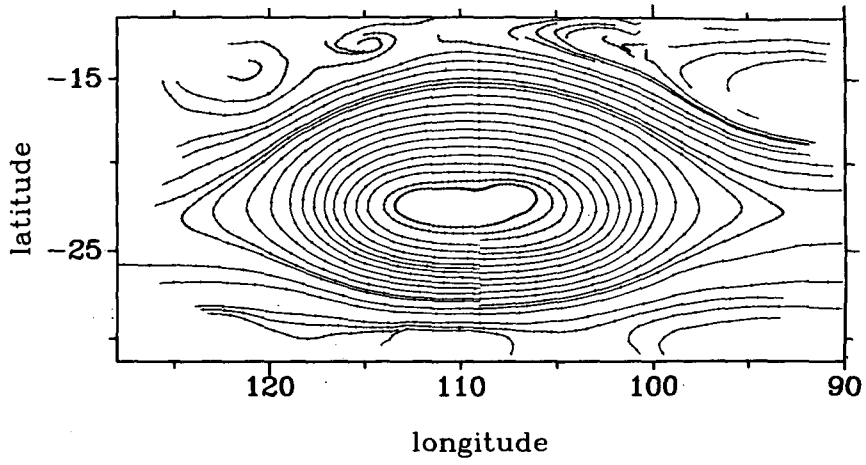

FIG. 3. Trajectories computed for the GRS. Small dots indicate intervals of 10 hours. The averaging box used to determine the local velocity was 3° by 3° in size.

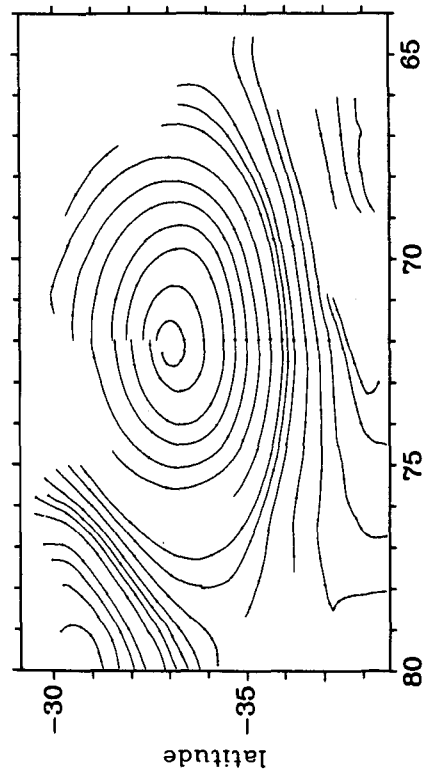

FIG. 5. As in Fig. 3 but for BC. The averaging box used to determine the local velocity field was 2° by 2°.

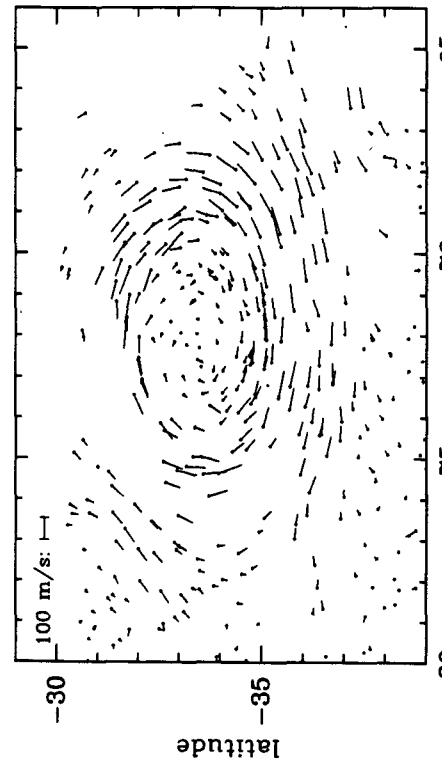

FIG. 4. As in Fig. 2 but for the White Oval BC. The zero of longitude corresponds to System III on 4 March 1979.

3. Method of analysis

From the measured velocity vectors (Figs. 2 and 4), we compute vorticity, divergence, and fluid trajectories. To do this we use an averaging box $2d$ on a side, and fit the data within the box to smooth functions of the form

$$u = A_1\phi + B_1\lambda + C_1, \tag{1}$$

$$v = A_2\phi + B_2\lambda + C_2, \tag{2}$$

where u and v are eastward and northward velocity components, respectively. A least-squares fit determines the A, B and C as well as the error covariance matrix. The optimum value of the box size $2d$ is a compromise between having a large number of measured points in the box and being able to resolve small-scale structures in the flow. A minimum of 10 points per box at most locations leads to $d = 1.5°$ for the GRS and $d = 1.0°$ for BC.

Vorticity and divergence are linear functions of the velocities and velocity gradients and are therefore linear functions of the A, B and C. For an oblate spheroidal planet with $\epsilon = R_e/R_p$ the expressions involve the radii of curvature in the zonal and meridional directions, which are

$$r(\lambda) = R_e(1 + \epsilon^{-2}\tan^2\lambda)^{-1/2}, \tag{3}$$

$$R(\lambda) = R_e\epsilon^{-2}(r/R_e\cos\lambda)^3, \tag{4}$$

respectively. Using the identity $\partial r/\partial\lambda = -R\sin\lambda$ we find for the vorticity ζ and the horizontal divergence $D = \nabla\cdot v$

$$\zeta = -\frac{1}{R}\frac{\partial u}{\partial\lambda} + \frac{u}{r}\sin\lambda + \frac{1}{r}\frac{\partial v}{\partial\phi}, \tag{5}$$

$$D = \frac{1}{R}\frac{\partial v}{\partial\lambda} - \frac{v}{r}\sin\lambda + \frac{1}{r}\frac{\partial u}{\partial\phi}. \tag{6}$$

Throughout this paper we use east longitude in the equations and west longitude in the figures.

Trajectories are calculated by stepping forward in time, integrating the velocities u and v in Eqs. (1) and (2) to reach the next location. The center of the box and the point on the trajectory leapfrog over each other on alternate parts of the timestep. The equations to be integrated are

$$u = r\dot{\phi}, \quad v = R\dot{\lambda}. \tag{7}$$

Equations (1), (2) and (7) are written in the following form,

$$\frac{\phi_2 - \phi_1}{t_2 - t_1} = \frac{1}{r_1}\left(A_1\frac{\phi_1 + \phi_2}{2} + B_1\frac{\lambda_1 + \lambda_2}{2} + C_1\right), \tag{8}$$

$$\frac{\lambda_2 - \lambda_1}{t_2 - t_1} = \frac{1}{R_1}\left(A_2\frac{\phi_1 + \phi_2}{2} + B_2\frac{\lambda_1 + \lambda_2}{2} + C_2\right). \tag{9}$$

Equations (8) and (9) are solved for the coordinates of the new point on the trajectory (ϕ_2, λ_2) given the coordinates of the old point (ϕ_1, λ_1). The center of the

box is integrated an additional half step $(t_2 - t_1)/2$ past the new point. There, new velocity vectors are collected and the least squares program determines new values of the A, B and C. These values are substituted into Eqs. (8) and (9), and the process is repeated. The time step $(t_2 - t_1)$ is chosen so that the displacement is never more than 4 percent of d. Halving the time step has no effect on the trajectories.

Figures 6 and 7 are maps of ζ and its standard deviation σ_ζ, respectively, for the GRS. Figure 8 is a map of D for the GRS, and Fig. 9 is a map of ζ for BC. These maps are made by moving the averaging box around a latitude–longitude grid. The grid spacing is 0.5°, which is ⅓ of d for the GRS and ½ of d for BC. Locations where there are fewer than 10 measured velocity vectors inside the box are shown as black squares. Standard deviations σ_ζ and σ_D are computed from the error covariance matrix assuming uncorrelated measurement errors and a perfect model [Eqs. (1) and (2)]. These assumptions are discussed further in the next section. The standard deviation σ_D (not shown) has the same large-scale structure as σ_ζ and approximately the same root mean square (rms) amplitude (4.2×10^{-6} s^{-1} for σ_D vs 4.3×10^{-6} s^{-1} for σ_ζ). Other standard deviations and rms amplitudes are given in Table 1.

Our trajectory analysis requires that the flow be steady. This requirement is approximately satisfied in the reference frames of the GRS and BC but not in System III. The transformation involves knowing the drift rates $\dot{\phi}_d$ of these objects relative to System III. The 126-day interval between the *Voyager 1* encounter and the *Voyager 2* encounter provides the time base. The simplest method is to use color or albedo to define the object (GRS or BC). A better method for our purposes is to use the velocity data to define the object. An initial guess of the vortex drift rate is used to interpolate the *Voyager 1* velocity data onto a latitude–longitude grid which drifts at this rate. (The images in a pair are almost always 10 hours apart, but the *Voyager 1* pairs cover a 3 to 4 day period.) The same procedure is followed for the *Voyager 2* data. From the disagreement in position of the GRS between these two datasets we calculate a correction to the drift rate, and repeat the procedure until it converges. The first method (albedo plus color) was used for BC, since the BC velocity data are from *Voyager 1* only. The second method (velocities) was used for the GRS.

We find that BC drifted eastward relative to System III at an average rate of 0.392 ± 0.007 deg day^{-1}. The GRS drifted westward at an average rate of 0.258 ± 0.001 deg day^{-1}. Since the longitude of the GRS oscillates with a 90-day period (e.g., Smith and Hunt 1976), this average rate applies only to the time between the *Voyager* encounters. With these estimates of the drift rates, two changes were made to the original (ungridded) velocity data. First, the longitude of each vector was shifted into a single reference frame corresponding to System III on 5 July 1979 for the GRS and 4 March 1979 for BC. Second, the zonal velocity of each vector was incremented by $-r\dot{\phi}_d$, where r is evaluated at the latitude of the vector and $\dot{\phi}_d$ is the drift rate of the GRS or BC. At the latitude of the GRS center this velocity increment is 3.49 m s^{-1}. At the latitude of BC center the velocity increment is −4.84 m s^{-1}. We also noticed a 0.2° latitude shift between the *Voyager 1* and *Voyager 2* velocity data. Following Limaye (1986) we attribute the shift to a problem with *Voyager 1* image navigation, and have corrected the *Voyager 1* latitudes accordingly.

4. Error analysis

Errors of analysis and interpretation fall into three classes. The first class arises from the sampling strategy used to generate the wind vectors. The second class arises from measurement error and small-scale motions in Jupiter's clouds. The third class arises from the physical model, e.g., the assumption that potential temperature and potential vorticity are constant on trajectories. We assess the effects of the sampling strategy by applying it to a synthetic dataset constructed from a known velocity field. Measurement error and small-scale motions are modeled by adding a random velocity to the synthetic dataset. Our ability to recover the known velocity field from the synthetic dataset provides an estimate of measurement error. Integral constraints provide a partial check of the physical model.

For the synthetic velocity field, we choose a simple harmonic motion with closed elliptical trajectories. The ellipses are concentric and have a constant ratio $a/b = 2.1$ of semimajor axis to semiminor axis in degrees. The latter value is from Mitchell et al. (1981) and is based on observations. Each ellipse, identified by its semimajor axis, has its own frequency $\omega(a)$. Thus the coordinates $\phi(t, a)$ and $\lambda(t, a)$ of the fluid parcel are

$$\phi(t, a) = \phi_0 + a \cos\omega t, \tag{10}$$

$$\lambda(t, a) = \lambda_0 + a\left(\frac{b}{a}\right) \sin\omega t. \tag{11}$$

The velocity field $u(\phi, \lambda)$, $v(\phi, \lambda)$ is given by

$$u(\phi, \lambda) = (\lambda_0 - \lambda) r(\lambda)\left(\frac{a}{b}\right)\omega[a(\phi, \lambda)], \tag{12}$$

$$v(\phi, \lambda) = (\phi - \phi_0) R(\lambda)\left(\frac{b}{a}\right)\omega[a(\phi, \lambda)]. \tag{13}$$

To make the flow resemble the observed flow around the GRS (Mitchell et al. 1981), we choose

$$\omega(a) = \omega_0 \frac{\exp[-(a - a_0)^2/a_1^2] + a_2}{(1 + a_2)}, \tag{14}$$

with $\omega_0 = 1.1 \times 10^{-5}$ s^{-1}, $a_0 = 8.7°$, $a_1 = 3.9°$ and $a_2 = 0.1$.

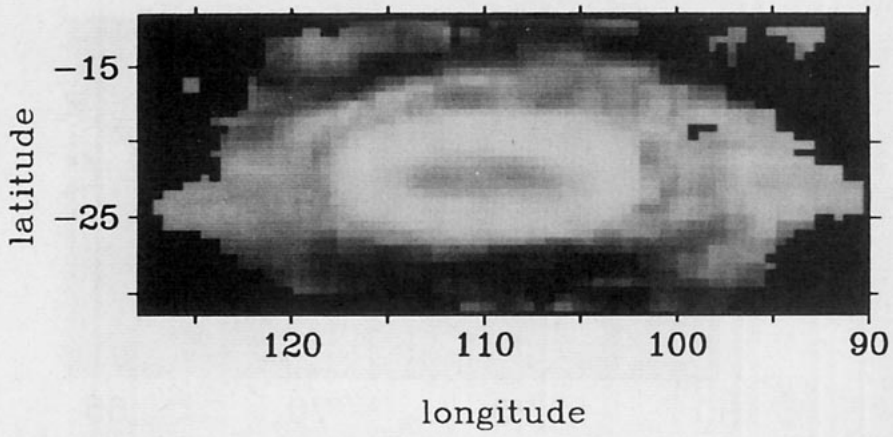

FIG. 6. Relative vorticity ζ of the GRS. Light shades correspond to positive ζ (anticyclonic in southern hemisphere) and dark shades correspond to negative ζ. The vorticity was calculated every 0.5° from the least squares fit to velocities inside a 3° by 3° box. The lightest and darkest shade (before black) equals the image mean plus and minus three image standard deviations, respectively. Black indicates less than ten data points available for computation. In this image the image mean is 0.4×10^{-6} s^{-1} and the standard deviation is 19.2×10^{-6} s^{-1}.

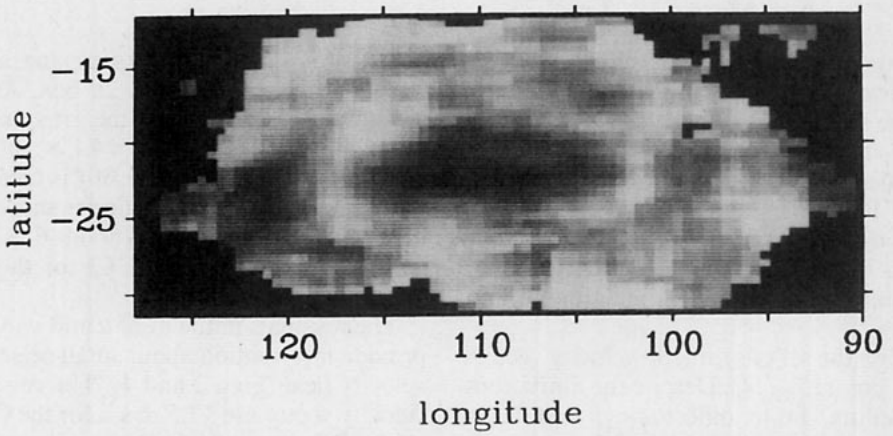

FIG. 7. Formal error map σ_ζ for the ζ in Fig. 6. The rms value of σ_ζ for this image is 4.3×10^{-6} s^{-1}. The lightest shade corresponds to 9.9×10^{-6} s^{-1} and the darkest shade before black corresponds to zero.

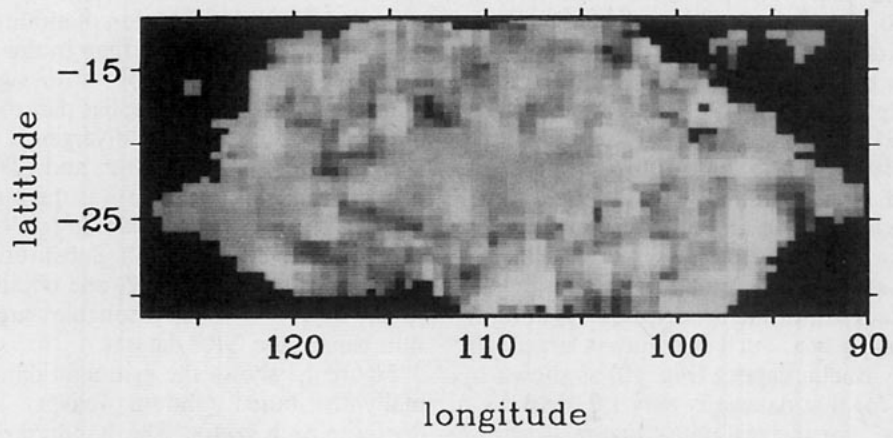

FIG. 8. Horizontal divergence D of the GRS. The shading is as in Fig. 6 but with a mean of -0.1×10^{-6} s^{-1} and a standard deviation of 4.8×10^{-6} s^{-1}.

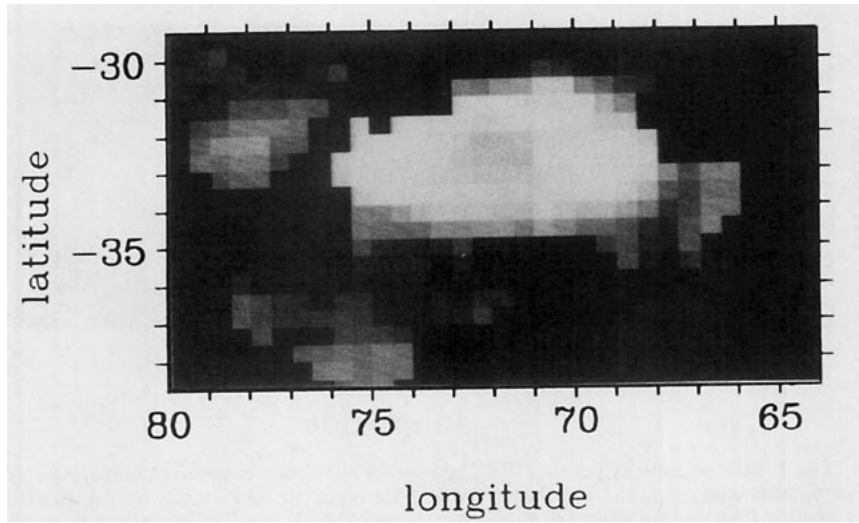

FIG. 9. As in Fig. 6 but for BC. The vorticity was calculated every 0.5° from the least-squares fit to velocities inside a 2° by 2° box. The shading is as in Fig. 6 but with a mean of 13.8×10^{-6} s^{-1} and a standard deviation of 36.6×10^{-6} s^{-1}.

To simulate the *Voyager* observation sequence we use the locations of the cloud features in the *Voyager* images, the same locations as those from which Fig. 2 was constructed. The features are displaced by increasing t in Eqs. (10) and (11) by the appropriate amount, usually around 10 hours. Velocity vectors are computed from the differences in position over the finite time interval, as in the real dataset. Vorticity and divergence are computed by least squares fitting to Eqs. (1) and (2).

Figure 10 shows the set of synthetic velocity vectors computed from Eqs. (10)–(14). Despite the limitations of uneven sampling, finite differencing, and least-squares averaging, trajectories computed from this dataset are near-perfect ellipses to an accuracy better than the line width. Figure 11 shows a map of $(\zeta_{true} - \zeta)$, the difference between ζ computed analytically from Eqs. (12) and (13) and ζ computed from the velocity vectors of Fig. 10. This error in ζ is dominated by large-scale structure. Its rms amplitude is 4.1×10^{-6} s^{-1}. For comparison, the quantity ζ that we are trying to measure has rms amplitudes of 19.2×10^{-6} s^{-1} for the GRS velocities (Fig. 2) and 15.9×10^{-6} s^{-1} for the synthetic velocities (Fig. 10).

Figures 7 and 11 show two parts of the same quantity, namely the uncertainty in our measurement of ζ. Figure 7 shows σ_ζ for the real dataset (Fig. 2). It measures the small-scale structure of the velocity field—structure that does not fit the model, Eqs. (1) and (2), inside the averaging box. Such structure is largely absent from the synthetic dataset (Fig. 10) as shown by the fact that σ_ζ for that dataset is only 1.0×10^{-6} s^{-1} (vs 4.3×10^{-6} s^{-1} for the real data). Figure 11 shows $(\zeta_{true} - \zeta)$ for the synthetic dataset. It measures the effects of finite differencing (displacements over 10 hours), non-uniform spatial sampling, and least squares averaging within the $2d \times 2d$ box. As mentioned in the preceding paragraph, the rms amplitude of the quantity shown in Fig. 11 is 4.1×10^{-6} s^{-1}. The total uncertainty in our estimate of ζ is taken to be the rms combination of the uncertainties shown in Figs. 7 and 11. This combined error is about 6×10^{-6} s^{-1}, which is 30% of the rms ζ and 6% of the total range of $(\zeta + f)$.

The residuals in the fit of u and v to Eqs. (1) and (2) provide information about small-scale structure in the velocity field (Figs. 2 and 4). The rms residuals of the velocity vector are 17.5 m s^{-1} for the GRS and 18.5 m s^{-1} for BC. About 85% of the variance σ_v^2 is associated with the downstream component of velocity. The remainder is associated with the cross-stream component. This anisotropy is probably due to the filamentary nature of the cloud patterns (Fig. 1). The features are stretched out in the direction of motion and are harder to locate in that direction than in the cross-stream direction. The fact that $\langle D^2 \rangle^{1/2}$ is not significantly larger than σ_ζ or σ_D (Table 1) implies that the velocity errors are uncorrelated and the divergence is small. Under such circumstances, σ_ζ^2, σ_D^2, and $\langle D^2 \rangle$ should all be of order $3\sigma_v^2/(Nd^2)$, where N is the number of vectors in the averaging box of side $2d$ ($\langle 1/N \rangle = 1/22$ for the GRS, $\langle 1/N \rangle = 1/14$ for BC). Substituting $\sigma_v = 17.5$ m s^{-1}, $d = 1800$ km, $N = 22$, one obtains $\sigma_\zeta \approx \langle D^2 \rangle^{1/2} \approx 3.6 \times 10^{-6}$ s^{-1}, in reasonable agreement with the numbers of the GRS dataset.

Figure 12 shows the synthetic dataset with a normally-distributed random velocity added independently to each vector. The standard deviation is 16.2 m s^{-1} in the component parallel to the large-scale flow and 6.7 m s^{-1} in the perpendicular component. This

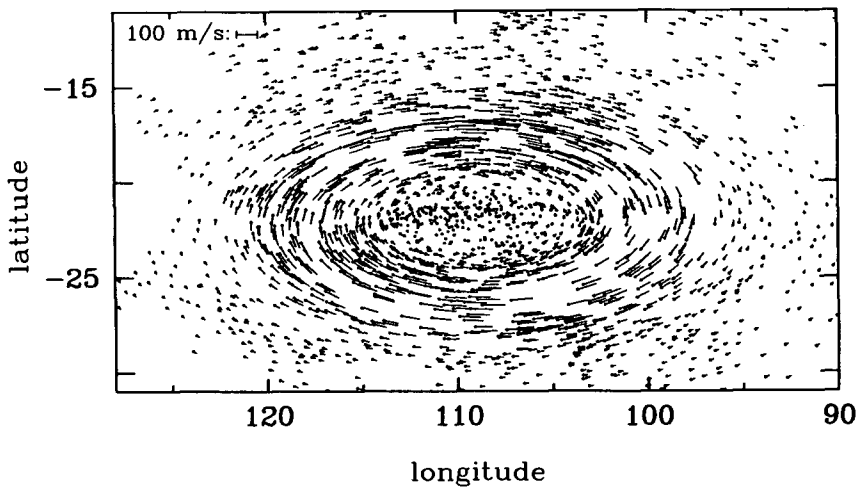

FIG. 10. Synthetic GRS-like velocity field. The velocities were computed by finite differencing an analytical function, Eqs. (10)–(14), using the mean positions and time intervals of the GRS data. Velocities are plotted as in Fig. 2.

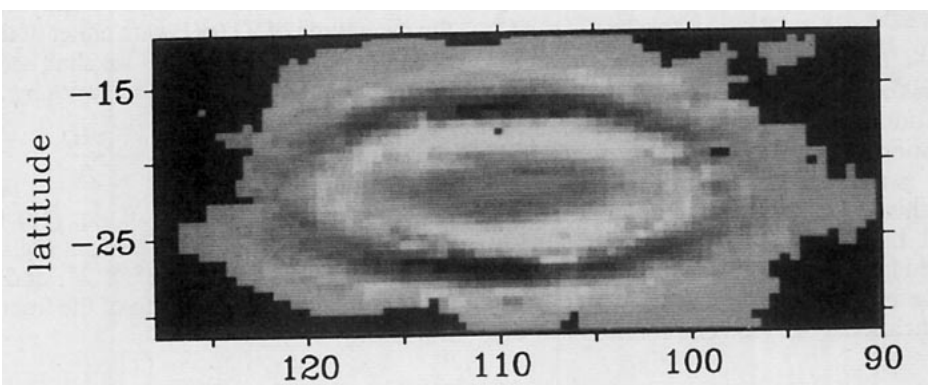

FIG. 11. The difference between the analytical vorticity ζ_{true} and the ζ recovered from the corresponding synthetic velocities in Fig. 10. The light and dark regions correspond to positive and negative values of $(\zeta_{true} - \zeta)$, respectively. The shading is as in Fig. 6 but with a mean of 0.3×10^{-6} s^{-1} and a standard deviation of 4.1×10^{-6} s^{-1}.

dataset has essentially all of the statistical properties of the GRS dataset (Table 1) and has the same general appearance as Fig. 2. Adding the random velocity isotropically (12.4 m s^{-1} in each component) has a distinctly noisier appearance. We conclude that the GRS velocity errors are essentially uncorrelated, lie mostly in the downstream direction, and have an rms magnitude of about 17.5 m s^{-1}. The BC velocity errors are also uncorrelated and directed downstream with an rms magnitude of 18.5 m s^{-1}.

5. Equations and integral constraints

Our interpretation of the data relies on the equations of motion with potential temperature θ as a vertical coordinate (e.g., Haltiner and Williams 1980). For large-scale (hydrostatic) flow of a stably stratified fluid ($H = -\partial P/\partial\theta > 0$), the continuity equation is

$$\frac{\partial H}{\partial t} + \nabla\cdot(\boldsymbol{v}H) + \frac{\partial}{\partial\theta}(\dot{\theta}H) = 0. \qquad (15)$$

Here $\boldsymbol{v}$ is the two-dimensional (horizontal) velocity, and $\dot{\theta}$ is the rate of change of θ following the fluid motion. For large-scale frictionless flow the vorticity equation is

$$\frac{\partial(\zeta + f)}{\partial t} + \nabla\cdot[\boldsymbol{v}(\zeta + f)] + \mathbf{k}\cdot\nabla\times\left(\frac{\dot{\theta}\partial\boldsymbol{v}}{\partial\theta}\right) = 0. \qquad (16)$$

If the flow is adiabatic then $\dot{\theta} = 0$, and the two equations may be combined to yield

TABLE 1. Standard deviations and rms amplitudes.

Figure	Quantity	Value
6	GRS $\langle \zeta^2 \rangle^{1/2}$	19.2
7	GRS σ_ζ	4.3
8	GRS $\langle D^2 \rangle^{1/2}$	4.8
	GRS σ_D	4.2
9	BC $\langle \zeta^2 \rangle^{1/2}$	39.1
	Synthetic $\langle \zeta^2 \rangle^{1/2}$	15.9
	Synthetic σ_ζ	1.0
	Synthetic $\langle D^2 \rangle^{1/2}$	1.1
11	Synthetic $\langle (\zeta_{\text{true}} - \zeta)^2 \rangle^{1/2}$	4.1
	Random $\langle \zeta^2 \rangle^{1/2}$	16.4
	Random $\langle D^2 \rangle^{1/2}$	4.6
	Random σ_ζ, σ_D	4.4

Note: Units are 10^{-6} s^{-1}. The headings GRS, BC, Synthetic, and Random refer to the data in Figs. 2, 4, 10 and 12, respectively.

$$\frac{\partial}{\partial t}\left(\frac{\zeta + f}{H}\right) + \boldsymbol{v} \cdot \nabla\left(\frac{\zeta + f}{H}\right) = 0. \tag{17}$$

Equation (17) is the conservation of potential vorticity for large-scale, adiabatic, frictionless flow.

One implication of the above equations with $\partial/\partial t = 0$ and $\dot{\theta} = 0$ is that every trajectory must close on itself. To see this, consider a trajectory that spirals slowly outward. Let C be one cycle of the trajectory—an almost-closed loop with a short section S across the place where the ends fail to join. Integrate Eq. (15) over the area enclosed by $C + S$. The second term can be turned into a surface integral, and since $\boldsymbol{v}$ is parallel to C the entire (positive definite) contribution comes from S. If $\partial/\partial t = 0$ and $\dot{\theta} = 0$, the contribution from S must vanish and the trajectories must be closed.

Since the trajectories of Figs. 3 and 5 fail to close by small amounts, we can use the above argument to estimate the possible importance of the $\partial/\partial t$ and $\dot{\theta}$ terms. The average of the second term in Eq. (15) over the domain is

$$|\nabla \cdot (\boldsymbol{v}H)| \sim \frac{v_s H_s D_s}{A_{C+S}}, \tag{18}$$

where v_s, H_s and D_s are velocity, thickness, and distance, respectively, across the short section S, and A_{C+S} is the area enclosed by $C + S$. If the flow were steady and adiabatic then Eq. (15) would give $\nabla \cdot (\boldsymbol{v}H) = 0$, whence

$$H\nabla \cdot \boldsymbol{v} + \boldsymbol{v} \cdot \nabla H = \nabla \cdot (\boldsymbol{v}H) = 0. \tag{19}$$

This relation is essential for deriving Eq. (17), the conservation of potential vorticity. We can estimate the extent to which the relation is violated by comparing the magnitude of $\nabla \cdot (\boldsymbol{v}H)$ with either of the other terms in Eq. (19), e.g., $\boldsymbol{v} \cdot \nabla H$. As we shall see, H varies by its own magnitude as latitude varies by 20°. Thus

$$|\boldsymbol{v} \cdot \nabla H| \sim \frac{vH}{L}, \tag{20}$$

where L is 20°. The ratio of Eq. (18) to Eq. (20) is therefore of order $D_s L / A_{C+S}$. From Fig. 3 we estimate $D_s \sim 0.1°$, $A_{C+S} \sim \pi \times 8° \times 3°$, and so $D_s L / A_{C+S} \sim 0.03$, which is an estimate of the fractional error in Eq. (19).

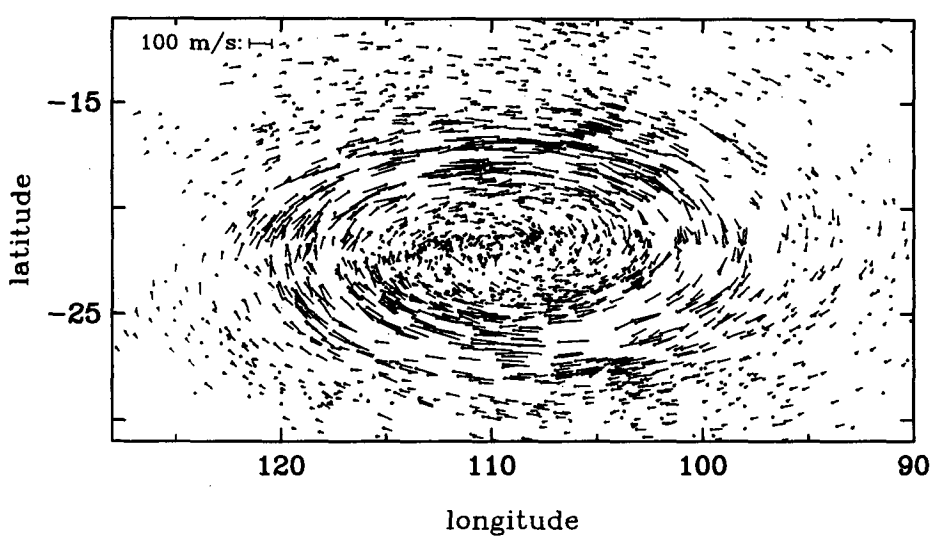

FIG. 12. Synthetic velocity field with noise. This is the same as Fig. 10 except gaussian noise is added to the positions used in the finite difference velocity calculation. The standard deviation of this noise in terms of velocity is 17.5 m s^{-1}, with 85 percent of the variance associated with the downstream component and 15 percent associated with the cross-stream component. This random dataset has $\sigma_\zeta \approx \sigma_D \approx \langle D^2 \rangle^{1/2} = 4.6 \times 10^{-6}$ s^{-1}, which is close to the values for the real dataset (Table 1).

Most or all of the spiraling in Figs. 3 and 5 is simply due to error in the velocity measurement. Applying our trajectory algorithm to the synthetic velocity field with noise (Fig. 12) gives as much spiraling as in the real dataset. Without noise, the synthetic dataset (Fig. 10) gives much less spiraling than the real dataset. Spiraling could also arise from poorly-resolved small-scale eddies, time-dependent motions, or motions across potential temperature surfaces. Spiraling could arise if the observed velocity vectors were from different altitudes, that is, from different potential temperature surfaces. The integrated effect of these processes is no larger than the 3% error in Eq. (19), a negligible effect. However we cannot rule out local errors that are larger than the 3% value, provided such errors cancel out when the integral around the trajectory is taken.

Equation (19) can also be used to estimate the magnitude of the horizontal divergence D, since

$$D = \nabla \cdot v = -v \cdot \nabla \log H \sim v/L, \qquad (21)$$

where L is 20° as before. From Fig. 3 we estimate that the maximum meridional displacement is 1.7° in 10 hours ($v \sim 54$ m s^{-1}), whence $v/L \sim 2.4 \times 10^{-6}$ s^{-1}. Since $\log H$ increases poleward at the latitude of the GRS, we expect positive D on the east side and negative D on the west side. This large-scale pattern, which we measure indirectly by observing vorticity changes, is barely discernible in the divergence map, Fig. 8. In a regression analysis of the Fig. 8 data, the large-scale pattern implied by Eq. (21) shows up with 90% of its expected amplitude. However the rms amplitude of the divergence in Fig. 8 is 4.8×10^{-6} s^{-1}, and is apparently dominated by small-scale noise.

6. Results

In this section we show how $(\zeta + f)$ varies along trajectories. Such variations must be associated with variations in H since $(\zeta + f)/H$ is constant on trajectories. The magnitude of the constant is unknown, so we will focus on relative changes, i.e., changes of $\log|\zeta + f|$. We will discuss the magnitude of the variations as well as any obvious patterns that repeat from one trajectory to the next.

Figure 13 shows a set of trajectories around the GRS, condensed from Fig. 3. The trajectories are labeled a–h. The variation of $(\zeta + f)$ around each trajectory is shown in Fig. 14. Latitude is used to identify position on the trajectory, the left and right sides of Fig. 14 referring to the left and right sides of the trajectory, respectively. The gently curving dashed line is f as a function of latitude. Each curve is offset from the one below it by 75×10^{-6} s^{-1}. Figures 15 and 16 show a similar set of curves for BC, the trajectories for which are labeled *a–f*.

The first conclusion is that the relative changes of $(\zeta + f)$ vs. latitude are the same for all trajectories despite their different longitudes. That is, except for small-scale noise and a different scaling factor for each trajectory, the different curves in Fig. 14 could be sections of the same smooth curve. A similar statment holds for the curves of Fig. 16. One can compare the curves both across the figures and down the figures. In the former case one observes that on each trajectory a parcel returns to the same value of $(\zeta + f)$ as it crosses the same latitude on the east and west ends of the oval. In the latter case one observes that parcels on different trajectories j at different longitudes ϕ experience the same relative variations of $(\zeta + f)$ as they cross the same latitude λ. The solid curves represent $\log|(\zeta + f)/f_0| = (A\lambda^2 + B\lambda + Cj)$, with the same values of A and B used for the whole figure [Eq. (22), below]. The congruence of the curves with the data points argues that the derivatives $(\partial \log|\zeta + f|/\partial\lambda)_j$ measured at the same latitude but on different trajectories j at different longitudes ϕ are the same.

The mathematical statement of this conclusion is that $(\zeta + f)$ can be approximately represented by a separable function $G_j\hat{H}(\lambda)$ of trajectory and latitude. Since $(\zeta + f)/H$ depends only on j, it follows that H can also be represented by a separable function $E_j\hat{H}(\lambda)$ with the same latitude dependence $\hat{H}(\lambda)$. Stated differently, the conclusion is that $(\partial \log|\zeta + f|/\partial\lambda)_j$ is approximately independent of longitude, and can therefore be represented both at the center of each vortex and at its east and west ends by the same function $\partial \log\hat{H}/\partial\lambda$. This is one way to organize the data of Figs. 14 and 16. A slightly different way, based on a physical model, is discussed in the next section.

The second important conclusion is that the latitudinal variations of thickness are dynamically significant: The slopes $\partial \log\hat{H}/\partial\lambda$ are typically larger than $\partial \log f/\partial\lambda$. Good examples are the poleward parts of GRS trajectories *d–f*, the poleward parts of BC trajectories *d–e*, and the equatorward parts of BC trajectories *c* and *f*. This fact means that the effect of thickness variation with latitude is typically greater than the effect of Coriolis parameter variation with latitude—the beta effect.

Third, there are important similarities in the distribution of slopes $\partial \log\hat{H}/\partial\lambda$ vs λ for the GRS and BC. The curvature $\partial^2 \log\hat{H}/\partial\lambda^2$ is positive in both cases. Following trajectories, thickness increases sharply with southern latitude (increasing toward the pole faster than $|f|$) on the poleward sides of the GRS and BC. Thickness increases at about the same rate as $|f|(\partial \log\hat{H}/\partial\lambda \sim \partial \log f/\partial\lambda)$ on trajectories that cross the central latitudes of the GRS and BC. Thickness is constant along trajectories on the equatorward side of the GRS and increases toward the equator on the equatorward side of BC. The data are not consistent for instance with models in which thickness varies linearly with latitude along trajectories. We will return to this point in the next section.

The fitted curves in Figs. 14 and 16 were constructed by the method of least squares. For either the GRS or

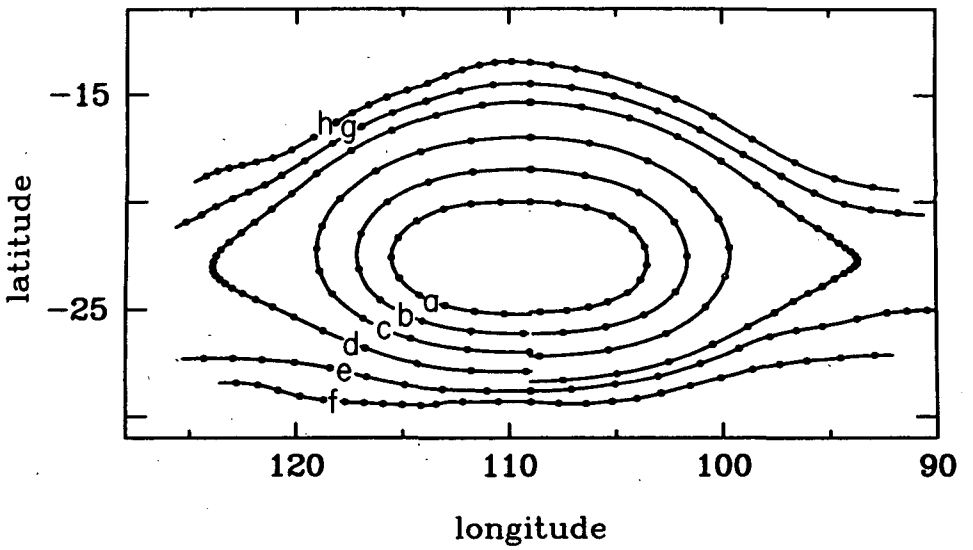

FIG. 13. Selected GRS trajectories. The trajectories shown here are a subset of those in Fig. 3 and are used in the potential vorticity analysis of Fig. 14. The dots indicate intervals of 10 hours.

BC, the value of $(\zeta + f)$ at latitude λ and on trajectory j is assumed to follow

$$\log\left[\frac{(\zeta + f)}{f_0}\right] = \log\hat{H}(\lambda) + C_j = A\lambda^2 + B\lambda + C_j. \quad (22)$$

The value of λ and the trajectory j are both functions of the point i at which ζ is measured. For N trajectories there are $N + 2$ constants to be determined. These are A and B, which determine $\partial \log\hat{H}/\partial\lambda$ for all trajectories, and the C_j which determine the ratios of the values of

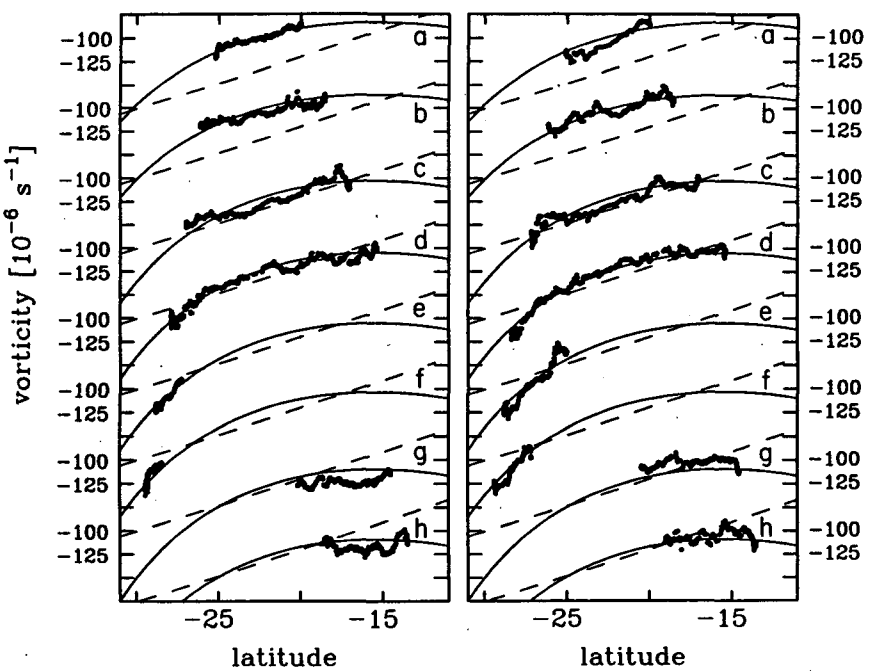

FIG. 14. Absolute vorticity $(\zeta + f)$ along trajectories versus latitude, for the GRS. Each $(\zeta + f)$ profile is labeled with a letter corresponding to a trajectory in Fig. 13. The left and right panels correspond to the trajectory segments left (west) and right (east) of 109° longitude, respectively. For each trajectory there are three pairs of curves, and these curves are offset from the next by 75×10^{-6} s^{-1} in the ordinate. The heavy dots are the computed $(\zeta + f)$. The gently sloping dashed curves are f. The solid curves are a least-squares fit to Eq. (22), namely $\log[(\zeta + f)/f_0] = A\lambda^2 + B\lambda + C_j$, where λ is planetographic latitude and j is the trajectory index.

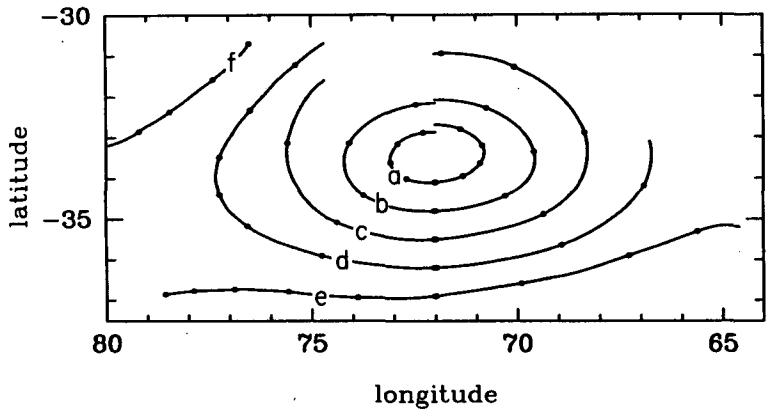

FIG. 15. As in Fig. 13 but for BC.

$|\zeta + f|$ on different trajectories at the same λ. The constant f_0 does not affect these ratios. For the GRS we choose $f_0 = 2\Omega \sin(-22.5°)$, and for BC we choose $f_0 = 2\Omega \sin(-33°)$.

Table 2 gives the results of this least squares analysis. Figures 17 and 18 show the data in the form $C_j - \log|\zeta + f|$. The smooth curve is the function $-A\lambda^2 - B\lambda$. The zero of the ordinate is arbitrary. The spread is due to several factors: small-scale variations on individual trajectories, lack of agreement between the left and right halves of the same trajectory, and large-scale structure that does not fit the quadratic form Eq. (22). Generally the spread is small enough so that the curve is well defined. For the GRS the ratio of the constant A to the formal uncertainty that comes from the least squares analysis is 7. For BC the ratio is 2.5. In other words the curvature is statistically significant. Similarly, on the poleward side of the GRS ($\lambda = -28.5°$) the magnitude of the slope $\partial \log\hat{H}/\partial\lambda$ is 13 times its formal uncertainty. On both sides of BC ($\lambda = -30°$, $\lambda = -36°$) the magnitude of the slope is 2 times its formal uncertainty.

In estimating uncertainty we assign a separate degree of freedom to each trajectory segment of length $2d$—the width of the averaging box. This procedure is consistent with our model of the error discussed in

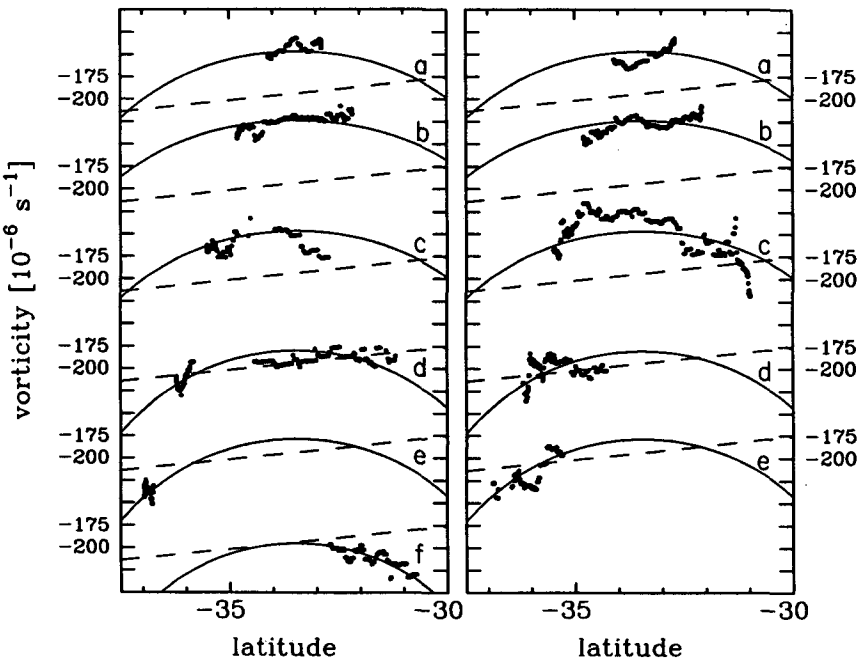

FIG. 16. As in Fig. 14 but for BC. The left and right panels correspond to the trajectory segments left (west) and right (east) of 72° longitude, respectively. The curves are offset 100×10^{-6} s^{-1} in the ordinate.

TABLE 2. Absolute vorticity vs latitude along trajectories fitted to Eqs. (22) and (27):

$$\log[(\zeta + f)/f_0] = A\lambda^2 = B\lambda + C_j$$

$$[(\zeta + f)/f_0] - 1 = A\lambda^2 + B\lambda + C_j.$$

Parameter (j = trajectory)	GRS		BC	
	(22)	(27)	(22)	(27)
A	11.06	13.16	82.72	82.46
B	5.93	7.61	96.60	96.40
C_a	0.314	0.693	27.93	27.94
C_b	0.343	0.710	27.76	27.81
C_c	0.523	0.865	27.93	27.93
C_d	0.545	0.892	28.14	28.12
C_e	0.546	0.914	28.13	28.13
C_f	0.529	0.913	28.21	28.18
C_g	0.587	0.918		
C_h	0.584	0.907		

Note: λ is planetographic latitude in radians ($\lambda < 0$), f_0 ($-22.5°$) $= -1.35 \times 10^{-4}$ s^{-1} for the GRS, f_0 ($-33°$) $= -1.92 \times 10^{-4}$ s^{-1} for BC.

section 4, where we showed to a good approximation that the velocity vectors of Figs. 2 and 4 have uncorrelated errors parallel to the local velocity. It follows for averaging boxes on the same trajectory that the autocorrelation of the residual of ζ falls linearly to zero as the distance between the box centers increases to $2d$. For averaging boxes on different trajectories the correlation is small (≤ 0.25) or zero when the separation between trajectories is either d, $2d$, or greater than $2d$. Since the separations in Figs. 13 and 15 are of order d, the errors from different trajectories are essentially uncorrelated. The residuals of the measured points in Figs. 14 and 16 are consistent with this model. That is, the equivalent width of the autocorrelation along a trajectory is of order $2d$, and the correlation from one trajectory to another is small.

Figures 14 and 16 show the results of the least-squares analysis in somewhat different form. Here the solid curves show $f_0 \exp(A\lambda^2 + B\lambda + C_j)$. Each of these curves is proportional to the function $\hat{H}(\lambda)$. Although the magnitude of this function is undetermined, its shape is well determined and is an important result of this paper.

7. Quasi-geostrophic model

In this section we study the implications of our observations in the context of a one-layer quasi-geostrophic (QG) model. The fluid has a free upper surface and rigid bottom topography that varies with latitude. The latter could represent either a curved solid surface, which is not a possibility for Jupiter's atmosphere, or a deep adiabatic fluid with a latitudinally varying zonal velocity. As we shall see, variable bottom topography is a required feature of the model if we are to fit the observed $(\zeta + f)$ variations. In fact the bottom must be curved locally downward near the GRS and BC so as to match the data of Figs. 14 and 16 at their respective latitudes.

For the large-scale flow that we have observed around the GRS and BC, the QG approximation is only good to the nearest 30% to 50%. Yet it fails rather uniformly. The three important terms in the vorticity equation—those involving ζ, f and H—all vary smoothly across the vortices and all contribute about equally to the balance. There is no special balance between 2 out of the 3 terms. We believe the next step after a QG model is a primitive equation model, at least for these large ovals on Jupiter.

Support for the above statements comes from Table 2 and Figs. 14 and 16. The values of $\exp(C_j)$ from Eq. (22) indicate how much $(\zeta + f)$ varies from one trajectory to another at the same λ. The ratio between the minimum and maximum values of $\exp(C_j)$ is 0.76 for the GRS and 0.64 for BC. For comparison, the ratio of the minimum and maximum H's on the same trajectory is 0.45 for the GRS (trajectory d) and 0.55 for BC (trajectory c). And the ratio between the minimum and maximum $|f|$ on the same trajectory is 0.55 for the GRS and 0.85 for BC. Not one of these numbers is particularly close to unity as required by the geostrophic approximation. But considering that these are extreme ratios (minimum to maximum), the QG approximation is useful at least in a semi-quantitative sense.

The fact that the model has only one layer is an obvious deficiency. Modeling the phenomenon of baroclinic instability requires at least two vertical degrees of freedom, for instance. The model also requires that we neglect vertical shears in the horizontal wind. However the *Voyager* infrared data (Gierasch et al. 1986) suggest that vertical shears are small in the upper troposphere (a few scale heights for the vertical scale), so the problem may not be serious. The free surface condition at the top is another deficiency. The rationale is that the pressure variation on a potential temperature surface in the stably stratified upper troposphere is small. In the lower troposphere where pressure is large and the static stability is small, the pressure variation on a potential temperature surface is large. The intervening layer should have a constant-pressure (stress-free) condition at the upper surface and a variable pressure at the lower surface. These problems in applying layer models to atmospheric flows are well known in terrestrial meteorology and are beyond the scope of this paper. The one-layer QG model with topography is at least a familiar one (e.g., Pedlosky 1987, §3.12 and 3.13), and has the minimum complexity needed to fit our potential vorticity data.

The QG vorticity equation for a single upper layer supported hydrostatically on a much deeper lower layer is

$$\frac{d}{dt}(\nabla^2\psi + f - k^2\psi + k^2\psi_2) = 0. \qquad (23)$$

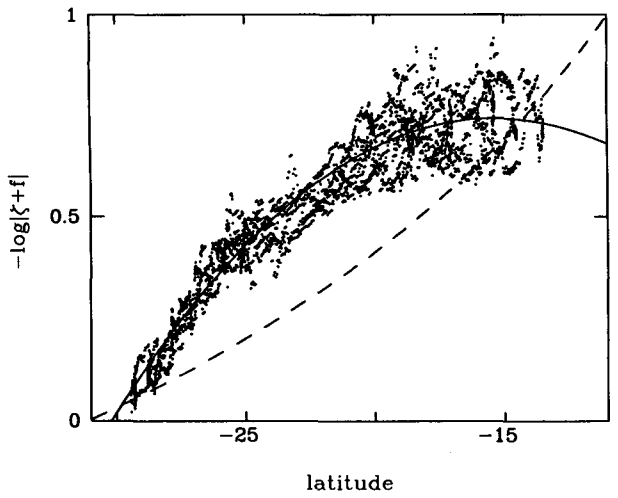

FIG. 17. Results of least squares fitting to the data of Fig. 14. The dots show the data in the form $C_j - \log|\zeta + f|$, the smooth curve is the fit to $-(A\lambda^2 + B\lambda)$, and the dashed curve is $-\log|f|$. The zero of the ordinate is arbitrary. Values of the constants A, B and C_j as used here and in Eq. (22) are given in Table 2.

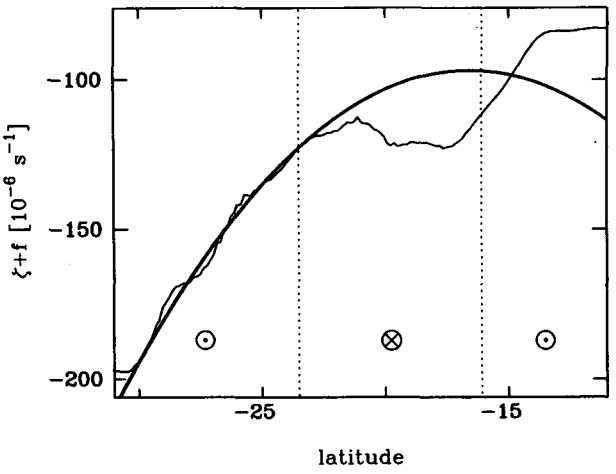

FIG. 19. Comparison of absolute vorticity variations along trajectories (this work) with zonal mean absolute vorticities in the vicinity of the GRS. The heavy curve is $(\bar{\zeta} + f)$ as given by Eq. (27) and Table 2. The light curve is $(\bar{\zeta} + f)$, computed from the high resolution zonal velocity profile of Limaye (1986). The vertical dotted lines indicate the zeros of zonal velocity in the GRS frame. The circles with dots indicate zonal velocities out of the page (eastward) and the circle with a cross indicates velocities into the page (westward). The zero of the ordinate for the heavy curve is arbitrary.

The dependent variable is the upper layer streamfunction $\psi(x, y, t)$, with velocities $u = -\partial\psi/\partial y$ and $v = \partial\psi/\partial x$. The equation was derived by Ingersoll and Cuong (1981), who used the notation $\bar{\psi}$ in place of ψ_2. The model differs from standard QG models only in the term $k^2\psi_2$, where $\psi_2(y)$ is the streamfunction of the zonal flow $u_2(y)$ in the lower layer. This term is absent when the lower layer is motionless with respect to the rotating coordinates or when the upper layer is supported by a solid surface which is horizontal in the rotating system. In general, ψ_2 could be a function of x, y and t, but our data suggest $\psi_2 = \psi_2(y)$. The terms in Eq. (23) are the QG vorticity $\zeta = \nabla^2\psi$, the Coriolis parameter $f = f_0 + \beta y$, a term $-k^2\psi$ from the free surface condition $P = 0$, and the term $k^2\psi_2$ from the condition that P be continuous across the lower interface. The constant k^2 is given by

$$k^2 \equiv \frac{1}{L_D^2} = \frac{f_0^2}{gH_0}\left(1 - \frac{\rho_1}{\rho_2}\right)^{-1}, \qquad (24)$$

where L_D is the radius of deformation, g is the gravitational acceleration, H_0 is the mean thickness of the upper layer, ρ_1 is its density, and ρ_2 is the density of the lower layer ($\rho_2 > \rho_1$). Because the lower layer is so much thicker than the upper layer, there is no feedback of upper layer motions on the lower layer dynamics. Thus if $\psi_2(y)$ is initially constant, it will remain so.

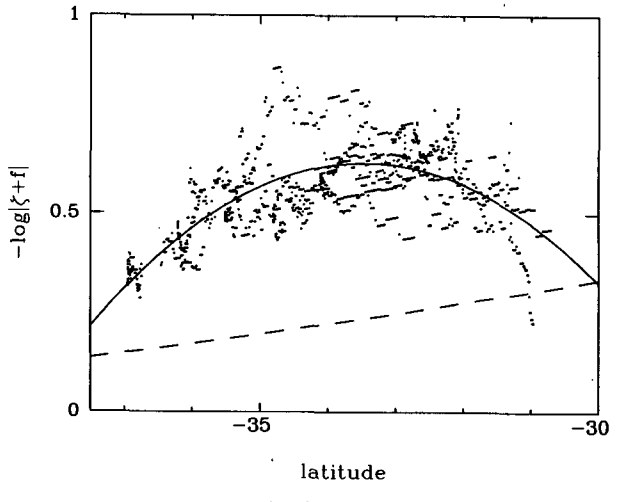

FIG. 18. As in Fig. 17 but for BC.

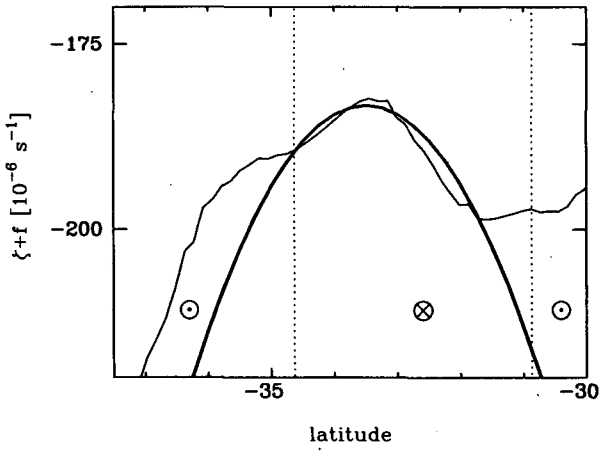

FIG. 20. As in Fig. 19 but for BC.

In the QG approximation the thickness variations along trajectories arise exclusively from motions in the deep lower layer. To show this we use the reference frame of the vortex where the flow is steady. Then Eq. (23) has a first integral

$$(\nabla^2\psi + f - k^2\psi + k^2\psi_2) = F(\psi). \tag{25}$$

This can be written

$$(\zeta + f) = -k^2\psi_2(y) + G(\psi), \tag{26}$$

where $G(\psi) = F(\psi) + k^2\psi$. Steady trajectories are lines ψ = constant. Therefore the curves in Figs. 14 and 16 are the QG approximation to $-k^2\psi_2$, where ψ_2 is the lower layer streamfunction in the reference frame of the vortex. The fact that the large-scale derivatives of the $(\zeta + f)$ curves in Figs. 14 and 16 depend much more on latitude than on longitude implies that ψ_2 is a function of y only, to a good approximation.

Exactly the same argument as the step from Eq. (25) to Eq. (26) is made by Pedlosky (1987, §3.13). To quote: "Each fluid element preserves its value of ψ and hence experiences no tube stretching due to the upper surface, which could, as far as the dynamics is concerned, be flat. Note that the vortex tubes will be stretched if fluid crosses isolines of η_B." In Pedlosky's notation η_B is a scaled measure of the bottom elevation from a constant reference value. The scaling factor is proportional to f_0, which changes sign at the equator. In the southern hemisphere the bottom elevation varies directly as $-k^2\psi_2$. Equation (26) therefore offers a simple physical analogy for Figs. 14 and 16, which resemble altitude-latitude cross sections of an ocean with variable bottom topography. The top of the ocean is the horizontal line $(\zeta + f) = 0$. The bottom of the ocean is the measured $(\zeta + f)$ curve, which is negative and therefore represents the altitude of the bottom with respect to sea level. Where the measured curve reaches a maximum, as it does once at $\lambda = -16°$ and again at $\lambda = -33.5°$, the bottom elevation is large and the thickness (depth) is small. As shown in the next section, this washboard topography has an important effect on the dynamics.

Equation (26) is the QG analogue of Eq. (22). To make the analogy as close as possible we rewrite Eq. (26) in the form

$$\frac{\zeta + f}{f_0} - 1 = A\lambda^2 + B\lambda + C_j. \tag{27}$$

Equations (22) and (27) become equal as $(\zeta + f)$ approaches f_0. The constants A, B and C_j of Eq. (27) are determined from the data by the method of least squares. These constants are listed in Table 2 for comparison with those of Eq. (22). Our estimate of $-k^2\psi_2$ is then given by the expression $f_0(A\lambda^2 + B\lambda)$.

According to Eq. (26), where $(\zeta + f)$ slopes upward to the right (λ or y increasing) the zonal flow in the lower layer is positive ($u_2 = -\partial\psi_2/\partial y$), and vice versa. Figure 14 shows that u_2 is eastward (positive) on the poleward side of the GRS and weak or westward (negative) on the equatorward side. Similarly Fig. 16 shows that u_2 is eastward on the poleward side of BC and westward on the equatorward side. In these respects the zonal flow in the lower layer resembles that in the upper layer.

One major result of this study is that the lower layer is in differential rotation—zonal velocity varies with latitude. If the rotation of the lower layer were uniform and if the vortex drifted westward, the velocity $u_2 = -\partial\psi_2/\partial y$ would be a positive constant. The $(\zeta + f)$ profiles in Figs. 14 and 16 would then be straight lines sloping upward to the right. The fact that the observed $(\zeta + f)$ profiles are curved implies that the lower layer is not rotating uniformly.

The magnitude of u_2 is of order βL_D^2, according to Fig. 14 which suggests that $-k^2 d\psi_2/dy$ is of order df/dy. Ingersoll and Cuong (1981) point out that L_D (the same as k^{-1}) could have any value in the range from 500 to 5000 km. The wide range reflects the uncertainty in $\Delta\theta$, where $\Delta\rho/\rho \sim \Delta\theta/\theta$ is the fractional potential temperature difference over one scale height ($H_0 \sim R_g\theta/g$), R_g is the gas constant, and L_D^2 is $R_g\Delta\theta/f_0^2$ from Eq. (24). These estimates give u_2 in the range from 1 to 100 m s^{-1}, which is not a very useful result. However, the effect of u_2 on the upper-layer dynamics is a well-measured quantity given by the term $k^2\psi_2$ in Eq. (23).

8. Rossby wakes

The above observational results are generally consistent with the model of Ingersoll and Cuong (1981), who postulated that the lower layer flow was exactly equal to the upper layer flow far to the east or west of the vortex. The additional requirement $k^2L^2 > 1$, where L is the radius of curvature of the zonal velocity profile, then made the far field of the vortex decay exponentially to zero (Ingersoll and Cuong, p. 2070, second column). Exponential decay in x and y ensures that the vortex is compact. In contrast, oscillatory behavior in x and y allows the vortex to radiate energy in a standing Rossby wave (Rossby wake) that extends far downstream. Ingersoll and Cuong were looking for stable, compact vortices in their numerical model, so they favored the kind of topography that would give exponential decay. In this paper we will be guided by the data. Given that the solid curves of Figs. 14 and 16 are QG approximations to $-k^2\psi_2$, we shall examine the implications for vortex structure using Eqs. (23) and (26).

The $k^2\psi_2(y)$ term adds a washboard topography to the usual β-plane dynamics. If we linearize Eq. (23) about a steady zonal flow $\bar{u}(y)$ in the upper layer, we obtain for the perturbation streamfunction ψ' in the upper layer

$$\nabla^2\psi' + \left(\frac{\beta - \bar{u}_{yy} - k^2u_2}{\bar{u}}\right)\psi' = 0. \tag{28}$$

The flow is assumed to be steady in the reference frame of the vortex. Both $\bar{u}$ and u_2 are measured relative to that frame. Solutions are wavelike or exponential depending on whether the bracketed term is positive or negative.

According to observations, the k^2u_2 term is just as large as β and as $\bar{u}_{yy}$. From Eq. (26) and the fact that $u_2 = -\partial\psi_2/\partial y$, the numerator in Eq. (28) can be written

$$\frac{\partial}{\partial y}(\bar{\zeta}+f) - \frac{\partial}{\partial y}(\hat{\zeta}+f) \equiv \frac{\partial q}{\partial y}. \tag{29}$$

Here $\bar{\zeta} = -\bar{u}_y$ is the vorticity of the zonal flow in the upper layer at large distances from the vortex, and $\hat{\zeta}$ is the vorticity measured along trajectories, the ζ part of $(\zeta + f)$ plotted in Figs. 14 and 16. According to Eq. (28), where $\bar{u} > 0$ (eastward flow in the upper layer relative to the vortex), solutions in the far field will be exponential provided $\partial q/\partial y < 0$. Where $\bar{u} < 0$, solutions will be exponential provided $\partial q/\partial y > 0$.

Figures 19 and 20 show $(\bar{\zeta}+f)$ and $(\hat{\zeta}+f)$ for the GRS and BC, respectively. The data of Limaye (1986) were used for $\bar{\zeta}$, although the data of Ingersoll et al. (1980) give the same results. Zonal velocities at 15 adjacent latitudes in Limaye's Table 1 were fitted to quadratic functions. Vorticity was then computed from Eq. (5). The fit to Eq. (27) was used for $\hat{\zeta}$, although Eq. (22) gives the same results. The vertical lines in Figs. 19 and 20 show latitudes where $\bar{u}$ changes sign from eastward to westward. At latitudes where $\bar{u} > 0$, Eq. (28) has exponential solutions if the heavy curves $(\hat{\zeta} + f)$ slope upward to the right more strongly than the light curves $(\bar{\zeta}+f)$. This condition is satisfied on the poleward side of BC ($-35° > \lambda > -37°$) and is marginally satisfied on the poleward side of the GRS ($-23.5° > \lambda > -29°$). At latitudes where $\bar{u} < 0$, Eq. (28) has exponential solutions if the heavy curves $(\hat{\zeta} + f)$ slope downward to the right more strongly than the light curves $(\bar{\zeta}+f)$. This condition is marginally satisfied on the equatorward side of BC ($-31° > \lambda > -35°$) and is violated on the equatorward side of the GRS ($-16° > \lambda > -23.5°$).

The above statements need some qualification. The light curves exhibit more detail than the heavy curves largely because the measurement of $(\bar{\zeta}+f)$ allows more detail than that of $(\hat{\zeta}+f)$. Thus it is possible that a negative slope $\partial(\hat{\zeta}+f)/\partial\lambda < 0$ like that exhibited by the $(\bar{\zeta}+f)$ curve (Fig. 19) at $-17° > \lambda > -21°$ is hidden in the noise of the fit to the smooth $(\hat{\zeta}+f)$ curve (Fig. 17). Comparison with Fig. 14 shows, however, that $\partial(\hat{\zeta}+f)/\partial\lambda$ is positive at $-17° > \lambda > -21°$ for all trajectories except possibly for the left portion of trajectory *h*. Whether the exception is significant or not requires more data from the turbulent region to the west and north of the GRS where the left portion of trajectory *h* originates.

The observations are consistent with the basic idea of Ingersoll and Cuong that a nonuniform zonal flow in the deep lower layer affects the upper layer dynamics. Some quantitative features of their model are also consistent with observation. The way topography dominates over β on the poleward sides of the GRS and BC is a good example. With the proper choice of k^2, the zonal flow in the lower layer could be set equal to $\bar{u}$ in this region. However the agreement is not good on the equatorward sides. For example, the band from $-16°$ to $-23.5°$ is characterized by strong westward flow (relative to the GRS) in the upper layer, as observed in *Voyager* images. The topography we have inferred implies an eastward flow (relative to the GRS) in the lower layer at these latitudes. This is seen in Fig. 14 from the smooth curves, which are proportional to $-k^2\psi_2(y)$ according to Eq. (26). The fact that the curves slope upward to the right ($u_2 = -\partial\psi_2/\partial y > 0$) in the latitude band $-16° > \lambda > -23.5°$ implies that the deep zonal flow is eastward. This disagreement suggests that the GRS and BC are not as compact as postulated by Ingersoll and Cuong.

According to the above qualitative analysis of Eq. (28), the westward flow on the equatorward side of the GRS is the one most likely to have a wake. Certainly the filamentary regions (FRs) to the west and north of the GRS and other Southern Hemisphere ovals are wakelike. The FRs are extensive turbulent patches that extend downstream (westward) to distances of ten or more semimajor diameters (Smith et al. 1979a,b; Ingersoll et al. 1979; MacLow and Ingersoll 1986). Perhaps they are Rossby wakes, and perhaps they are an important part of the dynamics of the long-lived ovals. If the vortices are rapidly losing energy through the wakes, then there must be an equal source of energy. A more complete analysis with a more accurate model should help answer these questions.

Acknowledgments. We thank Glenn Flierl for helpful suggestions made while one of us (AI) was participating in the Summer Study Program in Geophysical Fluid Dynamics at the Woods Hole Oceanographic Institution. We thank Glenn Garneau and Reta Beebe for helping to prepare the data and two anonymous referees for their helpful suggestions. This research was supported by the Planetary Atmospheres Program of NASA and by *Voyager* Project funds.

REFERENCES

Beebe, R. F., A. P. Ingersoll, G. E. Hunt, J. L. Mitchell and J. P. Müller, 1980: Measurements of wind vectors, eddy momentum transports, and energy conversions in Jupiter's atmosphere from Voyager 1 images. *Geophys. Res. Lett.*, **7**, 1–4.

Ertel, H., 1942: Ein neuer hydrodynamischer Wirbelsatz. *Meteor. Z.*, **59**, 277–281.

Gierasch, P. J., B. J. Conrath and J. A. Magalhães, 1986: Zonal mean properties of Jupiter's upper troposphere from Voyager infrared observations. *Icarus*, **67**, 456–483.

Haltiner, G. J., and R. T. Williams, 1980: *Numerical Prediction and Dynamic Meteorology*. Wiley and Sons.

Hatzes, A., D. D. Wenkert, A. P. Ingersoll and G. E. Danielson, 1981: Oscillations and velocity structure of a long-lived cyclonic spot. *J. Geophys. Res.*, **86**, 8445–8449.

Holton, J. R., 1979: *An Introduction to Dynamic Meteorology.* second ed. Academic Press.

Ingersoll, A. P., and P. G. Cuong, 1981: Numerical model of long-lived Jovian vortices. *J. Atmos. Sci.*, **38,** 2067–2076.

——, R. F. Beebe, S. A. Collins, G. E. Hunt, J. L. Mitchell, P. Muller, B. A. Smith and R. J. Terrile, 1979: Zonal velocity and texture in the Jovian atmosphere inferred from Voyager images. *Nature,* **280,** 773–775.

——, ——, J. L. Mitchell, G. W. Garneau, G. M. Yagi and J.-P. Muller, 1981: Interaction of eddies and mean zonal flow on Jupiter as inferred from Voyager 1 and 2 images. *J. Geophys. Res.*, **86,** 8733–8743.

——, ——, B. J. Conrath and G. E. Hunt, 1984: Structure and dynamics of Saturn's atmosphere. *Saturn,* T. Gehrels and M. S. Matthews, Eds., University of Arizona Press.

Limaye, S. S., 1986: Jupiter: New estimates of the mean zonal flow at the cloud level. *Icarus,* **65,** 335–352.

——, H. E. Revercomb, L. A. Sromovsky, R. J. Krauss, D. Santek, V. E. Suomi, S. A. Collins and C. C. Avis, 1982: Jovian winds from *Voyager 2.* Part 1: Zonal mean circulation. *J. Atmos. Sci.,* **39,** 1413–1432.

Mac Low, M.-M., and A. P. Ingersoll, 1986: Merging of vortices in the atmosphere of Jupiter: An analysis of Voyager images. *Icarus,* **65,** 353–369.

Mitchell, J. L., R. F. Beebe, A. P. Ingersoll and G. W. Garneau, 1981: Flow fields within Jupiter's Great Red Spot and White Oval BC. *J. Geophys. Res.*, **86,** 8751–8757.

Pedlosky, J., 1987: *Geophysical Fluid Dynamics,* second ed. Springer-Verlag.

Smith, B. A., and G. E. Hunt, 1976: Motions and morphology of clouds in the atmosphere of Jupiter. *Jupiter,* T. Gehrels, Ed., University of Arizona Press.

——, L. A. Soderblom, T. V. Johnson, A. P. Ingersoll, S. A. Collins, E. M. Shoemaker, G. E. Hunt, H. Masursky, M. H. Carr, M. E. Davies, A. F. Cook II, J. Boyce, G. E. Danielson, T. Owen, C. Sagan, R. F. Beebe, J. Veverka, R. G. Strom, J. F. McCauley, D. Morrison, G. A. Briggs and V. E. Suomi, 1979a: The Jupiter system through the eyes of Voyager 1. *Science,* **204,** 951–972.

——, R. Beebe, J. Boyce, G. Briggs, M. Carr, S. A. Collins, A. F. Cook II, G. E. Danielson, M. E. Davies, G. E. Hunt, A. Ingersoll, T. V. Johnson, H. Masursky, J. McCauley, D. Morrison, T. Owen, C. Sagan, E. M. Shoemaker, R. Strom, V. E. Suomi and J. Veverka, 1979b: The Galilean satellites and Jupiter: Voyager 2 imaging science results. *Science,* **206,** 927–950.

Sromovsky, L. A., H. E. Revercomb, V. E. Suomi, S. S. Limaye and R. J. Krauss, 1982: Jovian winds from *Voyager 2.* Part II: Analysis of eddy transports. *J. Atmos. Sci.,* **39,** 1433–1445.

Yagi, G., J. Lorre and P. Jepsen, 1978: Dynamic feature analysis for Voyager at the Image Processing Laboratory. *Proc. of the Conf. on Atmospheric Environment of Aerospace Systems and Applied Meteorology,* Boston, Amer. Meteor. Soc.